APPLYING THE LATTICE BOLTZMANN EQUATION TO MULTISCALE FLUID PROBLEMS

The authors discuss the theory and application of the Lattice Boltzmann equation to multiscale physics in fluids. They present two examples relevant to real-life applications: airflow around an airfoil at high Reynolds numbers and reactive flow in micropores.

In the quest to model complex physical phenomena, overstating the need for simulational tools that can handle multiple space and time scales is hard. The capability of addressing problems across several length and time scales is a hallmark of modern computational science, the goal of which is to tackle issues that straddle various traditional disciplines of science and engineering. Some interesting examples of such phenomena that have received considerable attention recently are drug design, the brittle or ductile failure of structural materials, heterogeneous catalysis, and turbulent combustion. We have come to know computational schemes aimed at such complex applications that involve multiple levels of physical and mathematical descriptions as *multiscale methods*.

One approach to multiscale modeling methods is to integrate schemes, which usually apply to a single-scale regime. This approach's central issue is dealing with the "hand-shaking" regions: At these regions, the different schemes that handle individual scales need to exchange information in a way that is physically meaningful, mathematically consistent, and computationally efficient. Two-level schemes combing atomistic and continuum methods for crack propagation in solids, or strong shock fronts in rarefied gases, made their appearance in the early 1990s.[1–3] More recently, researchers have applied three-level schemes to study crack dynamics, combining a finite-element (FE) treatment of continuum mechanics in regions far from the crack, a molecular dynamics (MD) treatment of atomic motion near the crack, and a quantum mechanical (QM) description of bonding in the crack tip's immediate neighborhood.[4] This FE-MD-QM implementation represents a concrete example of composite algorithms—that is, methods that involve seamless interfaces between the different mathematical models associated with different physical levels of description.

An alternative approach is to explore methods that can host more than one physical level of description—for example, atomistic, kinetic, and fluid—within the same mathematical framework. A potential candidate is the *Lattice Boltzmann equation* method. The LBE is a minimal form of the Boltzmann kinetic equation in

1521-9615/01/$10.00 © 2001 IEEE

SAURO SUCCI
National Research Council, Italy
OLGA FILIPPOVA
Duisburg University, Germany
GREG SMITH AND EFTHIMIOS KAXIRAS
Harvard University

which all details of molecular motion are removed except those that are strictly needed to recover hydrodynamic behavior at the macroscopic scale—mass, momentum, and energy conservation.[5–11] The result is an elegant and simple equation for a set of discrete distributions $f_i(\mathbf{x}, t)$ describing the probability of finding a particle at lattice site $\mathbf{x}$ at time t with speed $\mathbf{v}_i = \mathbf{c}_i$. These discrete distributions relate to the standard one-body Boltzmann distribution function of continuum kinetic theory through the following expression:

$$f(\mathbf{x},\mathbf{v},t) = \sum_i f_i(\mathbf{x},t)\delta(\mathbf{v} - \mathbf{c}_i). \quad (1)$$

The LBE combines the power of continuum methods with the geometrical flexibility of atomistic methods: It propagates smooth information, the discrete populations $f(\mathbf{x}, \mathbf{c}_i, t)$, along simple rectilinear trajectories prescribed by the lattice directions. The LBE could potentially play a twofold function—as a telescope for the atomistic scale and a microscope for the macroscopic scale. These aspects are useful and continue to expand vigorously, even 10 years after the basic theory's inception, in both academic[12] and commercial environments.[13] However, as we tackle multidisciplinary problems of growing complexity, it's increasingly evident that we need to upgrade the method to extend the range of scales the LBE can access and to couple it downward or upward with micro- and macroscopic methods. This article offers a cursory view of efforts in both directions, but let's first review the LBE theory's salient features.

Basic LBE theory

This is the simplest and by now most popular form of the LBE (often referred to as the *lattice BGK*[14,15] for Bhatnagar, Gross, and Krook[16]):

$$f_i(\mathbf{x} + \delta_t \mathbf{c}_i, t + \delta_t) - f_i(\mathbf{x},t) = -\omega\delta_t\left[f_i(\mathbf{x},t) - f_i^e(\mathbf{x},t)\right] \quad (2)$$

where $f_i(\mathbf{x}, t) \equiv f(\mathbf{x}, \mathbf{v} = \mathbf{c}_i, t)$, $i = 1,n$ is the probability of finding a particle at lattice site $\mathbf{x}$ at time t, moving along the lattice direction defined by the discrete speed $\mathbf{c}_i$, and δ_t is the time unit. To recover faithful fluid dynamics, we must choose the set of discrete speeds so that it guarantees mass, momentum, and energy conservation as well as rotational invariance. Only a limited subclass of lattices satisfies these conditions. For example, in 3D space, the lattice that satisfies these conditions consists of one particle with speed zero, six particles with speed unity (connecting a cube's center to its nearest-neighbor face centers), and 12 particles with speed $\sqrt{2}$ (connecting the cube's center to its edge centers, as in Figure 1).

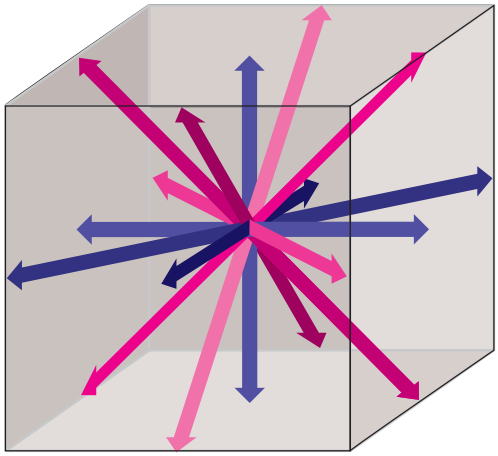

Figure 1. The set of discrete speeds in a 3D lattice. The set consists of one particle with zero speed represented by the cube center, six particles with speed unity represented by the arrows pointing to the centers of the cube faces, and 12 particles with speed $\sqrt{2}$ represented by the arrows pointing to the cube-edge centers.

In Equation 2, the left-hand side represents a forward discretization of the Boltzmann free-streaming operator

$$D_t \equiv \frac{\partial}{\partial t} + \mathbf{v}\cdot\nabla \quad (3)$$

along the discrete particle trajectories $d\mathbf{x}_i = \mathbf{v}_i dt$. The right-hand side represents intermolecular collisions in terms of an effective relaxation to a local equilibrium distribution f_i^{eq} in a time interval of the order ω^{-1}. This local equilibrium is usually taken in the form of a quadratic expansion of a Maxwellian

$$f_i^{\mathrm{eq}} = \rho w_i\left[1 + \frac{\mathbf{u}\cdot\mathbf{c}_i}{c_s^2} + \frac{\mathbf{uu}\cdot(\mathbf{c}_i\mathbf{c}_i - c_s^2 I)}{2c_s^4}\right], \quad (4)$$

where ρ is the fluid density, $\mathbf{u}$ the flow speed, and I the identity tensor; c_s is the lattice sound speed, defined by the condition

$$c_s^2 I = \sum_i w_i \mathbf{c}_i\mathbf{c}_i \quad (5)$$

and w_i a set of directional weights normalized to unity.

Local equilibria must obey the following conservation relations (for simplicity, we take the mass to be unity):

$$\sum_i f_i^{\mathrm{eq}} = \rho \tag{6}$$

$$\sum_i f_i^{\mathrm{eq}} \mathbf{c}_i = \rho \mathbf{u} \tag{7}$$

$$\sum_i f_i^{\mathrm{eq}} \mathbf{c}_i \mathbf{c}_i = \rho \left[\mathbf{u}\mathbf{u} + c_s^2 I \right] \tag{8}$$

In the limit of long wavelengths, where a particle's mean-free-path sets the scale, the fluid density and speed obey the Navier-Stokes equations for a quasi-incompressible fluid:

$$\frac{\partial \rho}{\partial t} + \nabla \cdot \rho \mathbf{u} = 0 \tag{9}$$

$$\frac{\partial \rho \mathbf{u}}{\partial t} + \nabla \cdot \rho \mathbf{u}\mathbf{u} = -\nabla P + \nabla \cdot [\mu (\nabla \mathbf{u})_S + \lambda (\nabla \cdot \mathbf{u}) I], \tag{10}$$

where $P = \rho c_s^2$ is the fluid pressure, $(\nabla \mathbf{u})_S$ is the symmetrized strain tensor, $\mu = \rho \nu$ is the dynamic viscosity, and λ is the bulk viscosity. For all practical purposes, we can neglect the last term involving the bulk viscosity when dealing with quasi-incompressible fluids. According to the definition of the pressure P, the LBE fluid obeys an ideal equation of state, which is reasonable because molecules, as represented by the LBE, have no potential energy. Using standard linear transport theory, with careful handling of artifacts the lattice introduces, the LBE fluid's kinematic viscosity becomes

$$\nu = c_s^2 \left(\frac{1}{\omega} - \frac{\delta_t}{2} \right). \tag{11}$$

The appearance of the factor $1/\omega$ in this expression is not surprising, because it corresponds to the relaxation time around local equilibria. In other words, c_s/ω is the lattice fluid's mean-free path. The factor $\delta_t/2$ is a genuine lattice effect, which results from an underlying Chapman-Enskog multiscale expansion. Fortunately, we can liken such a purely numerical effect to a negative viscosity. In particular, by choosing ω near and smaller than $\omega = 2/\delta_t$, we can achieve small viscosities, a basic prerequisite to simulating highly turbulent flows.

Historically, the LBE was derived as the one-body kinetic equation resulting from many-body lattice gas automata.[17] Here, we wish to motivate the LBE's physical meaning without delving into the details of its derivation. In doing so, we must invoke the values of certain dimensionless numbers that are typically employed in fluid dynamics. Table 1 defines all the dimensionless numbers mentioned in this article in terms of physical quantities relevant to fluid flow: l_m is the particle mean-free path, l_c is the flow's characteristic length, δ_x is the grid spacing (shortest fluid-dynamic length scale), u is the fluid velocity, c_s is the speed of sound in the fluid, ν is the kinematic viscosity, D is the diffusivity of the molecular species of interest, and τ_c is a characteristic time scale for chemical reactions. L and H are a tube's length and height and both represent macroscopic quantities.

The dimensionless numbers relevant to deriving LBE are the Knudsen number *Kn* and the Mach number *Ma*. The major conceptual steps in first deriving the LBE were low-*Kn* expansion around local equilibria and low-*Ma* expansion of the local equilibria around global equilibria. The low-*Kn* approximation corresponds to the standard picture of fluid dynamics as the mean-field approximation of kinetic theory in the limit of weak departures from local thermodynamic equilibrium. The low-*Ma* expansion is specific to the lattice framework. We can readily confirm that due to the finite number of discrete speeds, there is no way to fulfill the conservation constraints in Equation 4 with a Galilean-invariant local equilibrium of the form $f_i^{\mathrm{eq}} = f^{\mathrm{eq}}(\mathbf{v}_i - \mathbf{u})$ for a generic value of the fluid speed $\mathbf{u}$. However, expanding around global equilibria ($\mathbf{u} = 0$) and guaranteeing Galilean invariance term-by-term in the expansion is possible. Because the Navier-

Table 1. Definitions of dimensionless numbers mentioned in this article.

Name	Symbol	Definition	Description
Knudsen	*Kn*	l_m/δ_x	Ratio of particle mean-free path to shortest fluid dynamic scale
Mach	*Ma*	u/c_s	Normalization of fluid velocity u by speed of sound c_s in fluid
Reynolds	*Re*	ul_c/ν	Ratio of advective to dissipative effects
Peclet	*Pe*	uH/D	Ratio of advective to diffusive time scales
Damkohler	*Da*	$H^2/D\tau_c$	Ratio of diffusive to chemical reaction time scales

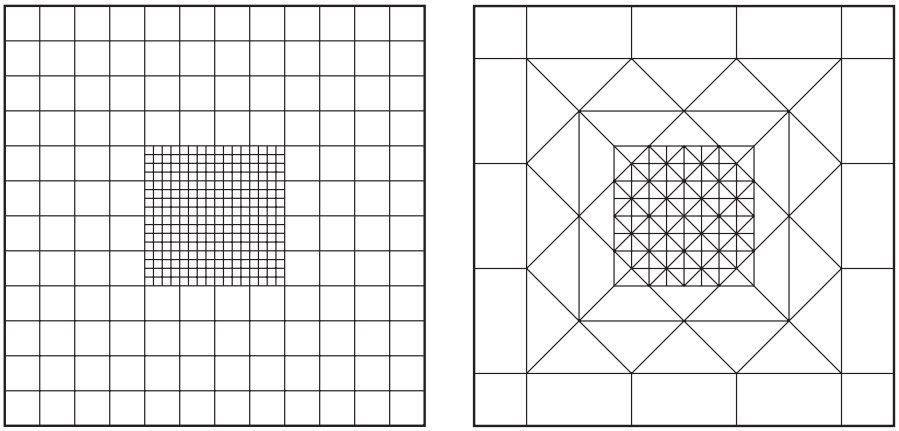

(a) (b)

Figure 2. (a) A locally embedded grid in which the local connectivity (in this example, four), is unchanged, but the lattice spacing is refined in the central region—the refinement shown is by a factor of four. (b) An unstructured grid in which the local connectivity as well as the spacing are varied—in this example, the connectivity ranges from five in the outer region to eight in the inner.

Stokes equations are quadratic in the fluid speed, a second-order expansion sufficiently fulfills this requirement but restricts the LBE approach's validity to low-*Ma*, quasi-incompressible flows. Researchers have developed modern variants dealing with high-*Ma* flows in recent years, but we aren't concerned with that in this article, nor will we discuss flows with thermal effects.

A few years after its introduction, researchers realized that they could obtain the LBE mathematically by standard projection of the continuum BGK equation on Hermite polynomials and subsequent numerical evaluation of the kinetic moments by Gaussian quadrature.[18] This alternative route highlights the role of the discrete speeds $\mathbf{c}_i$ as Gaussian knots and shows that Gaussian integration works as an effective importance-sampling device of velocity space. This property is indeed the key for capturing the complexities of hydrodynamic flows by means of only a handful of discrete speeds.

Multigrid Lattice Boltzmann simulations

Much of the LBE method's simplicity stems from the fact that within its formulation, discrete physical particles move and interact on a regular uniform lattice. Many phenomena of fundamental and practical interest—such as shocks, boundary layers, and thin interfaces—involve wide ranges of time and length scales. An accurate description of these phenomena on a mesh demands highly clustered grids that are locally adapted to the problem's physics. Unstructured grids—that is, grids in which the lattice coordination number might change from place to place—provide a powerful response to this need. They allow much stronger distortions of the computational grid at the expense of significantly more complex data structures. Another popular option comes from locally embedded grids—regular grids in which the local connectivity is unchanged but the lattice spacing is refined or coarsened locally, typically in steps of two for practical purposes. Figure 2 shows examples of unstructured and locally embedded grids.

Local embedding is a specific instance of a more general framework known as multiscale (or multigrid) algorithms. Other work has proposed multigrid LBE schemes,[19] and researchers have subsequently tested and validated for moderate and high Reynolds number flows around cylinders and blades.[20,21] Keep in mind that people used LBE schemes that had finer resolution in regions of larger gradients in commercial software for years,[13] and we have examples of several LBE schemes working on single-grid nonuniform meshes.[22–25] In what follows, however, we concentrate on LBE schemes with local embedding that use a specific algorithm, presented elsewhere.[19–21]

High-*Re* flows present a major challenge to computational physics mainly because of fluid turbulence. The range of active scales in a turbulent flow goes from the macroscopic length L down to the so-called Kolmogorov dissipative length l_d, at which point dissipation takes over and turbulence dies out. We can estimate the Kolmogorov length as $l_d \sim L\,[Re]^{-3/4}$, and because values of Re around 10^6 are commonplace in practical applications (for instance, a car moving at 100 Km/h), it is immediately evident that a fully resolved numerical simulation of flow past a car involves four to five decades in scale, namely $10^{12} - 10^{15}$ degrees of freedom. This is beyond the capabilities of any foreseeable electronic computer probably for decades to come

1. Move and collide F on coarse grid
2. For $k = 0, \ldots, n-1$:
   2.1. Interpolate F (Equation 18) on interface coarse-to-fine grid
   2.2. Scale F to f (Equation 17) on interface coarse-to-fine grid
   2.3. Using scaled interpolated values move and collide f
3. Scale back f to F on interface fine-to-coarse grid.

Figure 3. The algorithm for updating the populations F and f on the coarse and fine grids through Equations 17 and 18.

and explains why, for most practical purposes, we must resort to turbulence models based on closure approximations for the effects of unresolved scales on the resolved ones.

Regardless of whether we use turbulence models or fully resolved simulations, the need for selective clustering of computational degrees of freedom in the computational domain's hot spots remains, hence the motivation for multigrid simulations. The starting point for the multigrid LBE theory is the LBGK formulation of fluid dynamics.[14] Dividing the lattice spacing by a refinement factor n refines the grid. The kinematic viscosity, defined in the LBGK model's frame, depends on the lattice spacing δ_x:

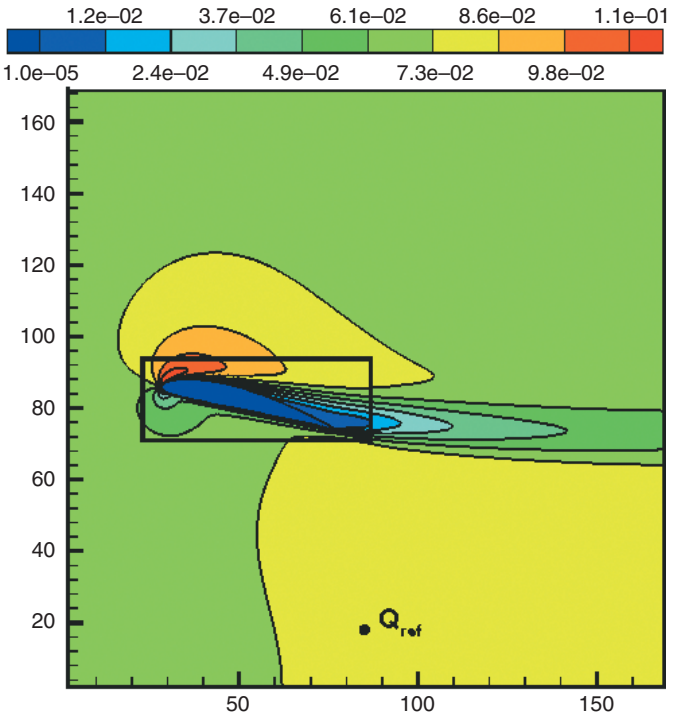

Figure 4. Modulus of the mean velocity $|\vec{u}|$ of the flow around the NACA 4412 airfoil at $Re = 1.5 \times 10^6$ and angle of attack $\alpha = 13.87°$. This calculation involves grid refinement between coarse and fine grids (the region for the latter indicated by the black rectangle) of $n = 5$. Q_{ref} denotes the point of reference for the pressure and velocity.

$$\nu = \frac{\delta_x c}{3\delta_t}\left(\frac{1}{\omega} - \frac{\delta_t}{2}\right). \tag{12}$$

To achieve the same viscosity on both coarse and fine grids, we must rescale the relaxation parameter in the LBGK scheme as

$$\omega_f = \left[\frac{\delta_t}{2} + n\left(\frac{1}{\omega_c} - \frac{\delta_t}{2}\right)\right]^{-1}, \tag{13}$$

where ω_f and ω_c are relaxation parameters on the fine and coarse grids, respectively, and n is the refinement parameter. We can split the discrete distribution function into equilibrium and nonequilibrium components:

$$f_i = f_i^{\mathrm{eq}} + f_i^{\mathrm{neq}}. \tag{14}$$

Using the LBGK equation, we can obtain the nonequilibrium component:

$$f_i^{\mathrm{neq}} = -\frac{1}{\omega}\left[\frac{\partial}{\partial t} + \mathbf{c}_i \cdot \nabla\right] f_i^{\mathrm{eq}} + \mathcal{O}\left([Kn]^2\right), \tag{15}$$

which is accurate to second-order $[Kn] = \delta_x/l_c$.

It is important to realize that the scale l_c can change significantly from place to place in the flow. The task of the multigrid method is precisely to adapt the grid resolution to this change of scales. In the low-frequency limit $\delta_t/\tau \sim [Kn]^2$, where τ is a typical hydrodynamic time scale,[19] the distribution function's nonequilibrium component simplifies to

$$f_i^{\mathrm{neq}} = -\frac{1}{\omega}\mathbf{c}_i \cdot \nabla f_i^{\mathrm{eq}} + \mathcal{O}\left([Kn]^2\right). \tag{16}$$

Combining this relation with the continuity of the hydrodynamic variables—and of their derivatives at the interface between the two grids—leads to this relation between the coarse and fine grid populations:

$$f_i' = \tilde{F}_i^{\mathrm{eq}} + \left(\tilde{F}_i' - \tilde{F}_i^{\mathrm{eq}}\right)\Omega^{-1} \tag{17}$$

$$F_i' = f_i^{\mathrm{eq}} + \left(f_i' - f_i^{\mathrm{eq}}\right)\Omega, \tag{18}$$

where capital symbols stand for coarse grid, primed symbols stand for post-collision, and symbols with a tilde stand for coarse-to-fine grid interpolation. The variable Ω is defined as

$$\Omega = n\frac{(1-\delta_t\omega_c)\omega_f}{(1-\delta_t\omega_f)\omega_c}. \tag{19}$$

The relations of Equations 17 and 18 define a mapping between coarse- and fine-grid distributions that clearly reduces to the identity in the limit $n \to 1$. We can cast these formal expres-

sions into an algorithm (see Figure 3): the algorithm's flow is straightforward, with the last step implementing the correction of the coarse-grid population with dynamic effects derived from the fine-scale grid. For steady-state flows, we can accelerate this algorithm by using only one subcycle ($n = 1$) in step 2.[26]

We recently coupled the multigrid LBE method with a finite-difference treatment of model equations for turbulence in relatively complex geometries such as high-*Re* flows past airfoils and compressor blades. Our goal was to develop a robust treatment of the boundary conditions between the turbulent fluid and the wall.[27] We used this coupled approach to study the flow around the NACA 4412 airfoil profile (a standard benchmark profile out of a suite provided by the National Advisory Committee for Aeronautics) by using a boundary-fitting formulation for wall functions through which the asymptotic solution describing near-wall turbulence is matched with simulation data outside the boundary layer.[21]

The flow geometry and parameters are defined elsewhere.[28,29] In our numerical simulations, we took into account the confined wind tunnel's blockage effect.[28] The numerical experiment is as follows: The flow is injected at the inlet in x direction with $Ma = 0.07$ and angle of attack $\alpha = 13.87°$ with respect to the inclined airfoil. We impose slip conditions on the computational domain's lower and upper boundaries. We extrapolate the pressure at these sections and at the inlet along the normal to the sections from the outer flow, while we assume that the pressure at the outlet is constant and the velocity is extrapolated along the normal from the outer flow. The Reynolds number value $Re = 1.5 \times 10^6$ is related to the length of the chord l_c, which, in the present example, is given by $l_c = 50\delta_x^c$, where δ_x^c is the coarse grid's spacing. The trailing edge's position in respect to the lower-left corner of the computational domain is $27.4391\delta_x^c$, $73\delta_x^c$. The computational domain consists of 170×170 nodes. We apply grid refinement—defined by the parameter $n = \delta_x^c/\delta_x^f$, where δ_x^f is the fine-grid spacing—to a box ($66\delta_x^c$, $25\delta_x^c$) surrounding the profile with the lower-left corner ($22\delta_x^c$,$70\delta_x^c$). The values of the relaxation parameters on the coarse and fine grids are $\delta_t\omega_c = 1.9$, $\delta_t\omega_c = 1.8$, resulting in the artificial numerical viscosity stabilizing the solution of inviscid flow.[18] The spacing between the slip surface (where boundary conditions are applied), and the airfoil's geometrical surface is uniform and equal to $0.0036\, l_c$.

Figure 4 shows the velocity magnitude $|\vec{u}|$ and streamlines in the whole computational domain for the case $n = 5$. Figure 5 shows the surface scaled-pressure distribution, defined as

$$C_P = 2\frac{P - P_{ref}}{\rho|\vec{u}_{ref}|^2}, \tag{20}$$

where P_{ref}, $\vec{u}_{ref}$ are values at a chosen reference point, as obtained numerically with the LBE code (for $n = 5$ and $n = 7$), as well as from a different simulation[28] and from experiment.[29] Besides a general agreement in the far-field region, we see a certain discrepancy between the numerical and experimental results near the pressure peak at the airfoil's leading edge—the development of laminar and transitional local flow regimes hampers a fully turbulent treatment of the boundary. The correct treatment of such critical regions is a standing challenge for current computational aerodynamics.

To date, the LBE method has proven competitive with state-of-the-art unstructured adaptive finite-volume formulations while retaining a significantly simpler computational structure. Much

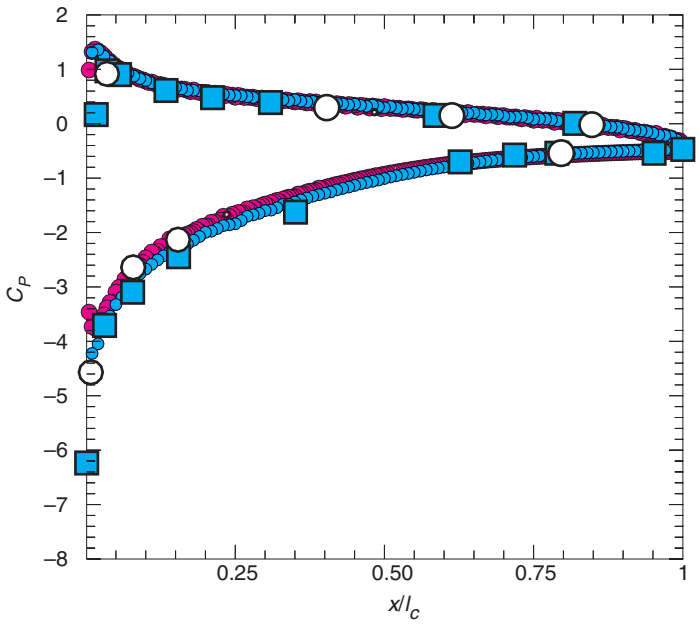

Figure 5. Surface scaled pressure C_p distribution for NACA 4412 airfoil at $Re = 1.5 \times 10^6$ and angle of attack $\alpha = 13.87^0$, as a function of scaled position x/l_c along the airfoil cord. The small magenta dots represent results from our runs with grid refinement between coarse and fine grids $n = 5$, while the small blue dots correspond to grid refinement $n = 7$. The large white circles are numerical results,[28] and the large blue squares are experimental data from other research.[29]

Table 2. Conversion efficiency η, defined in Equation 21, of the 2D reactive channel flow as a function of the Peclet (*Pe*) and Damkohler (*Da*) numbers.

τ_c (chemistry)	D (diffusion)	*Pe*	*Da*	η
10^2 (faster)	10^{-1} (faster)	50	250	0.47
10^2 (faster)	10^{-2} (slower)	500	2,500	0.18
10^3 (slower)	10^{-1} (faster)	50	25	0.09
10^3 (slower)	10^{-2} (slower)	500	250	0.07

work remains to be done to assess whether multigrid LBE simulations can take the lead in this important sector of computational aerodynamics.

Coupling to macroscopic grids

The LBE method can easily couple to finite-difference–volume–element methods for continuum partial differential equations partly because of its small time steps and geometrical flexibility. For example, take a millimetric flow with, say, 100 grid points per side, yielding a mesh spacing $\delta_x = 10$ microns. Assuming a sound speed of the order of 300 m/s, we obtain a time step of order $\delta_t = 30 \times 10^{-9}$ sec = 30 nsec. Such a small time step permits the handling of relatively fast reactions without having to resort to implicit time stepping, thus avoiding the solution of large systems of algebraic equations. The LBE's flexibility is especially suited to heterogeneous catalysis, because the simplicity of particle trajectories permits the description of fairly irregular geometries and boundary conditions.

Because of these two advantageous features, many researchers are using the LBE method to simulate reactive flows over microscopically corrugated surfaces—an application of great interest for the design of chemical traps, catalytic converters, and related devices.[30]

The general problem of a fluid flow carrying chemical species over a reactive surface is central to a variety of industrial and technological applications, such as the design of catalytic converters for cars. An important quantity in these systems is the chemical efficiency

$$\eta = 1 - \frac{\Phi_{out}}{\Phi_{in}}, \tag{21}$$

where Φ_{out} and Φ_{in} are the chemical fluxes at the inlet (where the chemical species is injected) and the outlet of the fluid domain, respectively. Here we consider 2D reactive flows to understand how the system's efficiency is affected by the geometry, diffusivity, and surface reaction of the chemical species at the catalytic wall. The concentration of the chemical species obeys a convection-diffusion equation of the form

$$\frac{\partial C}{\partial t} + \mathbf{u} \cdot \nabla C = D\nabla^2 C + R\delta(\mathbf{x} - \mathbf{x}_w), \tag{22}$$

where C is the density of the reactive species (pollutant) passively advected by the flow, D is the pollutant's molecular diffusivity, and R is a catalytic reaction term that is only active at the solid wall boundary, labeled w.

In engineering practice, the fluid-wall chemical interaction is expressed with a simple empirical rate equation,

$$\frac{dC_w}{dt} = \frac{C_f - C_w}{\tau_w} - \frac{C_w}{\tau_c}, \tag{23}$$

where the subscripts w and f stand for the wall and fluid cells that exchange mass, and τ_w and τ_c denote typical time scales for fluid-to-wall mass density transfer and chemical reactions, respectively—for simplicity, we take $\tau_w = \tau_c$. The relevant fluid scales are the advective transit time scale $\tau_A = L/u$ and the cross-channel diffusive time scale $\tau_D = H^2/D$, where H and L are the channel's height and length. These time scales define the major dimensionless parameters that control the conversion efficiency—that is, the *Pe* and *Da* numbers, which in this case take the form

$$Pe = \frac{uH}{D} = \frac{L}{H}\frac{\tau_D}{\tau_A}, \qquad Da = \frac{H^2}{D\tau_c} = \frac{\tau_D}{\tau_c}. \tag{24}$$

Because pollutant molecules must make it to the wall to be chemically consumed, high chemical efficiencies of the device go with low-*Pe* and high-*Da* values. On the other hand, for fluids moving at sizeable speeds—say, tens of meters per second—molecular diffusivity is generally too small to achieve sufficiently small *Pe* values. This motivates the use of corrugations to enhance the fluid-to-wall mass transfer and increase conversion efficiency. The corrugations that can be manufactured into a channel are by necessity of macroscopic dimensions. Their effect must be coupled to the microscopic scale at which diffusion and chemical reactivity take

place. We solve the fluid flow equations in the Lattice Boltzmann form, whereas we handle the reaction-diffusion equation for the chemical species with a modified Lax-Wendroff finite-difference scheme on a simple nearest-neighbor square lattice.[31]

The channel is 50 grid units high and 300 units long. With a lattice spacing of $\delta_x = 10$ microns, this gives a channel of dimensions 3 mm × 0.5 mm. We align the x-axis along the channel's length and the z-axis along its height. We choose initial conditions as follows: The flow is initialized at a uniform density $\rho = 1$ and speed $u_x = u_0$, $u_y = 0$, $u_z = 0$, with u_0 a constant throughout the fluid domain. The reactant concentration is initially zero everywhere. Boundary conditions for the flow are periodic at the inlet/outlet and no-slip (zero fluid speed) at the top and bottom rigid walls. The chemical reactant is continuously injected at the inlet with a constant profile $C(x = 0, y) = 1$ and flows freely away from the flow domain at the outlet section. At the top and bottom walls the reactant concentration obeys the dynamic boundary condition implied by the rate Equation 23.

To illustrate the LBE's capabilities, let's look at four pairs of simulations, with combinations of the values $\tau_c = 10^2$ or $\tau_c = 10^3$ and $D = 10^{-2}$ or $D = 10^{-1}$. We will refer to the simulations with the lower value of τ_c as the faster chemistry simulations and to those with the higher value of τ_c as the slower chemistry simulations. Similarly, we will refer to the simulations with the higher value of D as the faster diffusion simulations and those with the lower value of D as the slower diffusion simulations. We use the terms faster and slower to reflect the comparative changes in the system because, in all cases, chemical interactions take place on a rather fast pace compared to advection. For each set of parameter values, one simulation uses a smooth channel and the other a channel with a trapezoidal obstacle that is seven grid units high: the longer (bottom) base of the trapezoid is between grid points 119 and 176, and the shorter (top) base is between grid points 125 and 170. In all flows, the Reynolds number is $Re = uH/\nu \approx 500$, the Peclet number takes the values $Pe = 50$, 150, and 500, and the Damkohler number takes the values $Da = 25$, 250, and 2,500. The simulations last 3×10^5 time steps, which corresponds to about 10^{-2} seconds. This is longer than the longest diffusive time scale, and we chose it to ensure that we achieve steady-state conditions for both flow and species configurations. Table 2 summarizes these results.

Not surprisingly, the simulations with the faster chemistry and diffusion show the highest efficiency, $\eta = 0.47$. When we reduce D by an order of magnitude, the efficiency decreases to 0.18. The difference between the faster and slower diffusion simulations is not as pronounced in the case of slower chemistry ($\tau_c = 10^3$)—the efficiency is 0.09 and 0.07 in the two cases, respectively. In the slower chemistry simulations, diffusion is always fast enough to get the chemical species to the wall, but the bottleneck is waiting for the wall to consume the pollutants before advection sweeps them away.

For a given set of D and τ_c values, there is a small but significant difference between the efficiencies of the smooth channel and the channel with the obstacle. Figure 6 compares the concentration of the pollutant along the channel with and without the obstacle, and Figure 7 shows a more detailed look at the differences in concentration in the two geometries (for the faster chemistry case). Figure 6 shows the overall

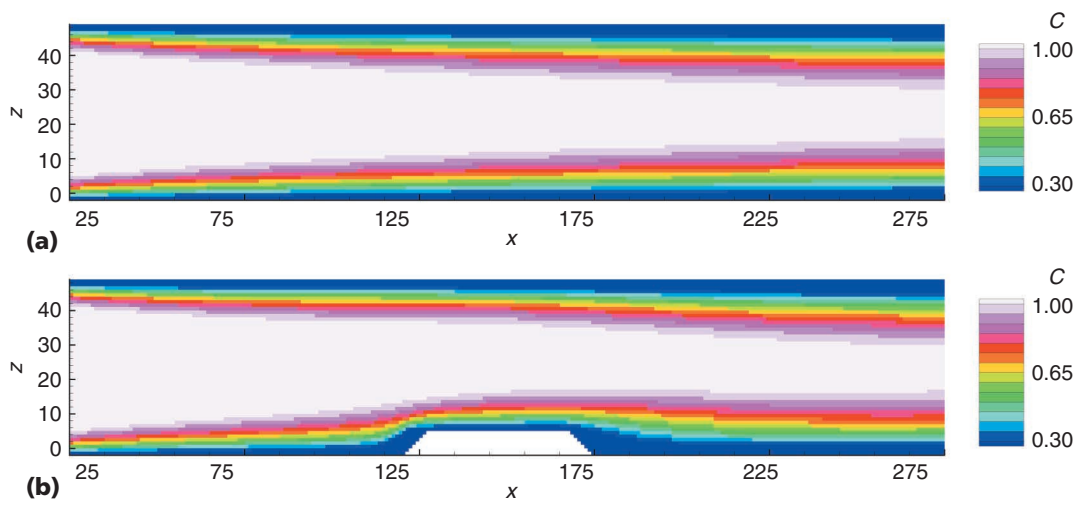

Figure 6. Concentration C of chemical species along the length of the smooth (a) and corrugated (b) channels. Near the top and bottom walls—particularly around the obstacle—the concentration falls markedly from its initial value.

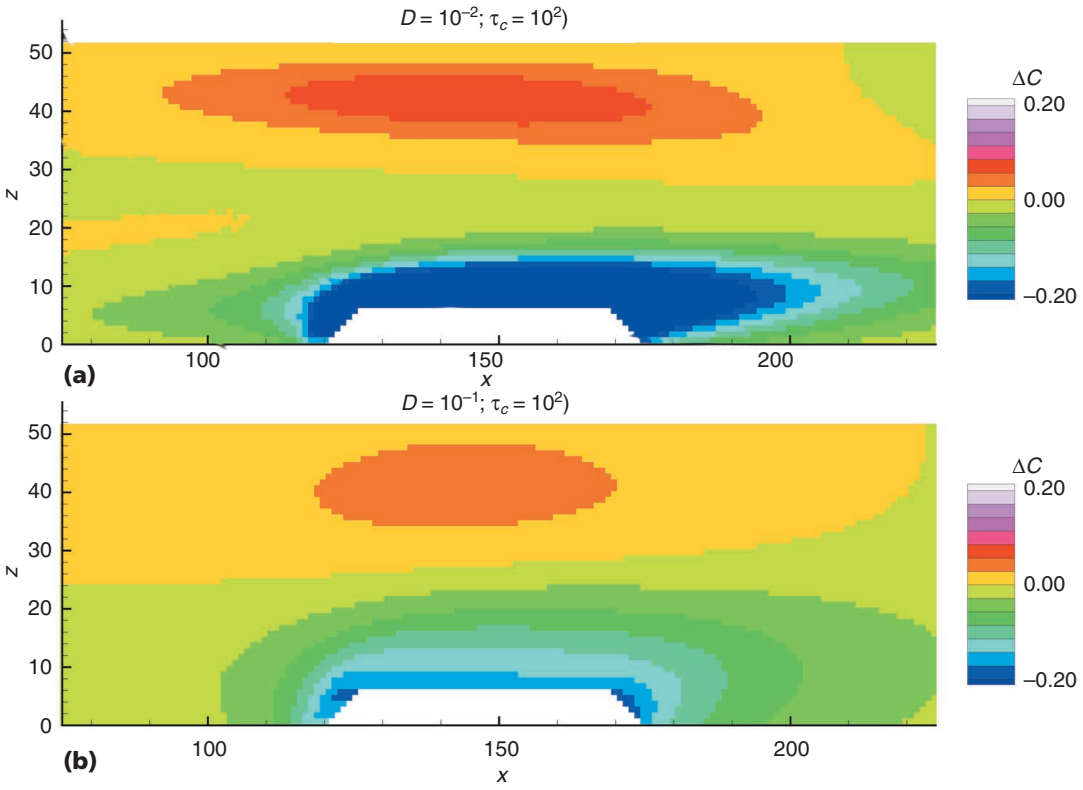

Figure 7. The difference in concentration ΔC of the chemical species in the fluid, between the smooth and corrugated channels, for the faster chemistry simulations ($\tau_c = 10^2$), at slower (a) and faster (b) diffusion. Only a portion of the channel along its length is shown, close to the trapezoidal obstacle.

effect of the obstacle in the concentration, which on this scale is indeed small. Figure 7 indicates the spatial distribution of changes in the concentration ΔC due to the obstacle's presence: a negative value of ΔC indicates lower concentration in the corrugated channel. As Figure 7 shows, the concentration is significantly reduced in the neighborhood of the obstacle (the small increase in concentration in the region far above the obstacle is an effect for the conservation of the total pollutant in the two simulations). Remarkably, the changes in concentration are as pronounced in front of the obstacle as behind it. There is also a significant change in concentration at the top surface of the obstacle. The results for the slower chemistry simulations are qualitatively similar but involve less pronounced changes between the smooth and corrugated channels.

To gain a more quantitative picture of where along the channel length the difference in efficiency originates, Figure 8 shows the difference in flux between the smooth and corrugated channels as a function of x, the position along the channel. The flux is defined as the concentration integrated along the vertical z direction at a given value of x, normalized by the channel cross section. The flux difference is actually small in the two simulations—less than 1 percent at any point along the channel. In all cases, a positive flux difference develops before the corrugation, an effect that is much more pronounced in the faster chemistry simulations. This results from the perturbation of the flow field far from the obstacle. Although the channel is four times longer than the obstacle, near the inlet and the outlet the velocity field has a vertical component with a magnitude approximately 10^{-5} of the maximum velocity in the x direction. This small perturbation, coupled with the rapid chemical reactions at the wall, results in the flux difference's initial rise.

Figure 8 indicates that the flux difference begins decreasing just before the front of the obstacle. This does not appear to be due to enhanced absorption in the wall in front of the obstacle. In fact, the values of the concentration at the wall indicate that the difference in concentration between the two simulations decreases right before the beginning of the obstacle. Instead, this decrease appears to be the result of the chemical species diffusing within the bulk fluid toward the region above the corrugation where there is a relative deficit of chemical species concentration. Interestingly, the decrease begins earlier and has larger magnitude in the simulations corresponding to faster diffusion. Figure 8 also indicates that directly on top of the obstacle there is a steady decrease of the flux dif-

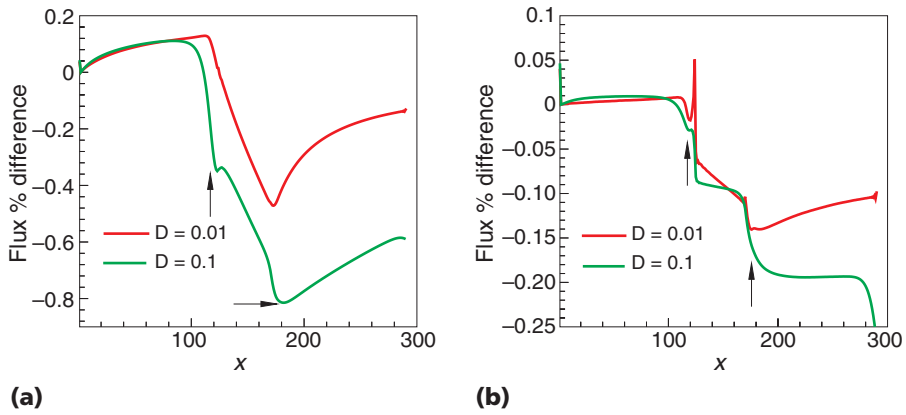

Figure 8. The percent difference in chemical species flux between smooth channel and corrugated channel simulations as a function of length *x* along the channel. A negative value indicates that the flux is smaller in the corrugated channel simulation. (a) $\tau_c = 10^2$ for the faster chemistry simulation, and (b) $\tau_c = 10^3$ for the slower chemistry simulation. The arrows mark the beginning and end of the obstacle.

ference, which results from the increase in concentration along the upper surface of the obstacle produced by the squeezing of hydrodynamic flow lines due to the obstacle's presence. Finally, after the obstacle, the flux difference begins increasing—most sharply in simulations with slower diffusion. We can expect that well beyond the extent of the obstacle the flux difference will tend to zero, because at that point the flow is similar in the smooth and corrugated channels. However, the smooth channel has a higher concentration of chemical species in that region due to the higher consumption of the pollutant around the obstacle, so the difference never quite reaches a zero value in the simulations.

These considerations give only a flavor of the type of questions that you can address by numerically simulating microreactive flows. Ultimately, the goal would be to map out a sensible expression of the chemical efficiency as a function of the relevant control parameters, which include the values of *Pe*, *Da*, and *Re* under arbitrary geometrical conditions. To this purpose, besides upgrading the computational techniques, a synergistic interplay with analytical scaling theories could also prove valuable.

The LBE method has already proven its remarkable versatility in addressing a wide range of problems that involve complex fluid motion at disparate scales. Multiscale simulations based on the LBE approach, two examples of which we discussed here, are just beginning to appear. There are good reasons to believe that further upgrades of the LBE technique as well as better communication with related fields of computational physics will make these types of multiscale applications flourish in the years to come.

Figure 9 gives a more concrete picture of our vision for future multiscale approaches. This

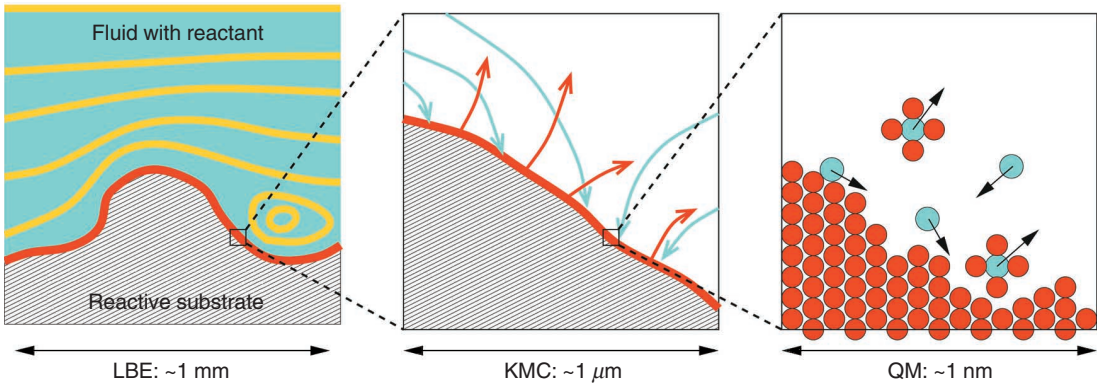

Figure 9. Illustration of combined multiscale LBE/KMC/QM scheme. In the LBE regime, the system length scale is ~ 1 mm, and the description is in terms of hydrodynamic fluid flows (gold lines). In the KMC regime the scale of the cell is ~ 1μm, and the description is in terms of fluxes of reactants (blue arrows) and reaction products (red arrows) determined by the diffusion, advection and chemical reactivity rates. In the QM regime, the scale of the cell is ~1 nm, and the description is in terms of individual molecules and atoms on the surface undergoing surface diffusion and chemical reactions.

type of problem is the epitome of multiscale physical phenomena[32] involving fluid motion and reactant transport at macroscopic scales, fluid-wall interactions at intermediate scales, and chemical reactions on the wall at microscopic scales. At the highest length scale, of order 1 mm, LBE-based simulations can handle the flow of fluids carrying macroscopic reactants around the substrate's geometric features. These simulations will determine the concentration fields of the reactants and reaction products. At the next lower scale, of order 1 μm, Kinetic Monte Carlo (KMC) simulations[33] will determine the flux of reactants toward the substrate and the flux of reaction products away from it—given the macroscopically determined concentration—as well as the reactivity and surface diffusion rates determined by microscopic considerations.

The LBE has already proven its remarkable versatility in addressing a wide range of problems.

At present, it is possible to determine a priori the rates for a range of relevant atomistic processes from ab initio quantum mechanical (QM) calculations and feed them into the KMC simulation.[34] We can then couple the KMC simulation to the LBE simulation in the manner discussed earlier. Ideally, we would like to be able to calculate the relevant atomistic rates on the fly, without having to make any assumptions about the likely events at this scale. The large computational cost of QM calculations makes this unfeasible at present as well as for the foreseeable future (barring some dramatic computational breakthroughs that could speed the QM calculations by many orders of magnitude). Methods for replacing the KMC-level simulations with actual MD simulations are the subject of current research,[35] but even those are not based on QM calculations of the energy and forces. It is nevertheless intriguing to imagine that multiscale simulations of the type outlined here will be carried out in the near future, offering insight into complex physical processes. Allowing for the possibility that we can realize this dream, the application to biologically related problems—where both the macroscopic geometric features of vescicles and the reaction of molecules at the microscopic level are of crucial importance—seems particularly promising.

Acknowledgments

This work was supported in part by the Materials Research Science and Engineering Center that the National Science Foundation funds at Harvard University. The NATO Collaborative Link Grant PST.CLG.976357 greatly facilitated the interaction between the authors. Sauro Succi thanks the Physics Department of Harvard University for his Visiting Scholar appointment and for its hospitality during his stay. We thank Achi Brandt for discussions on mathematical aspects of multiscale methods and Howard Stone for discussions on the physics of fluids.

References

1. W. Hoover, A.J. de Groot, and C. Hoover, "Massively Parallel Computer Simulation of the Plane-Strain Elastic-Plastic Flow via Non-Equilibrium Molecular Dynamics and Lagrangian Continuum Mechanics," *Computers in Physics*, vol. 6, no. 2, Mar./Apr. 1992, pp. 155–167.
2. E. Salomons and Mareschal, "Usefulness of the Burnett Description of Strong Shock Waves," *Physical Rev. Letters*, vol. 69, no. 2, July 1992, pp. 269–272.
3. S.T. O'Connell and P. Thompson, "Molecular Dynamics-Continuum Hybrid Computations: A Tool for Studying Complex Fluid Flows," *Physical Rev. E*, vol. 52, no. 6, Dec. 1995, pp. R5792–R5795.
4. F.F. Abraham et al., "Spanning the Length Scales in Dynamic Simulation," *Computers in Physics*, vol. 12, no. 6, Nov./Dec. 1998, pp. 538–546.
5. G. McNamara and G. Zanetti, "Use of the Boltzmann Equation to Simulate Lattice-Gas Automata," *Physical Rev. Letters*, vol. 61, no. 20, Nov. 1988, pp. 2332–2335.
6. F. Higuera and J. Jimenez, "Boltzmann Approach to Lattice Gas Simulations," *Europhysics Letters*, vol. 9, no. 7, Aug. 1989, pp. 663–668.
7. F.J. Higuera, S. Succi, and R. Benzi, "Lattice Gas-Dynamics with Enhanced Collisions," *Europhysics Letters*, vol. 9, no. 4, June 1989, pp. 345–349.
8. H.D. Chen, S.Y. Chen, and W.H. Matthaeus, "Recovery of the Navier-Stokes Equations Using a Lattice-Gas Boltzmann Method," *Physical Rev. A*, vol. 45, no. 8, Apr. 1992, pp. R5339–R5342.
9. R. Benzi, S. Succi, and M. Vergassola, "The Lattice Boltzmann Equation: Theory and Applications," *Physics Reports*, vol. 222, no. 3, Dec. 1992, pp. 145–197.
10. S. Chen and G. Doolen, "Lattice Boltzmann Method for Fluid Flows," *Ann. Rev. Fluid Mechanics*, vol. 30, 1998, pp. 329–364.
11. S. Succi, *The Lattice Boltzmann Equation for Fluid Dynamics and Beyond*, Clarendon Press, Oxford, UK, 2001.
12. X. Shan and H. Chen, "Lattice Boltzmann Model for Simulating Flows with Multiple Phases and Components," *Physics Rev. E*, vol. 47, no. 3, Mar. 1993, pp. 1815–1819.
13. A. Anagnost et al., *Digital Physics: Analysis of the Morel Body in Ground Proximity*, tech. report 970139, Int'l Congress and Exposition, Detroit, 1997.
14. S. Chen et al., "Lattice Boltzmann Model for Simulation of Magnetohydrodynamics," *Physical Rev. Letters*, vol. 67, no. 27, Dec. 1991, pp. 3776–3779.

15. Y.H. Qian, D. d'Humieres, and P. Lallemand, "Lattice BGK Models for Navier-Stokes Equation," *Europhysics Letters*, vol. 17, no. 6, Feb. 1992, pp. 479–484.
16. P. Bhatnagar, E. Gross, and K. Krook, "A Model for Collisional Processes in Gases I: Small Amplitude Processes in Charged and Neutral One-Component System," *Physical Rev. B*, vol. 94, no. 3, 1954, pp. 511–525.
17. U. Frisch, B. Hasslacher, and Y. Pomeau, "Lattice Gas Automata for the Navier-Stokes Equations," *Physics Rev. Letters*, vol. 56, no. 14, Apr. 1986, pp. 1505–1508.
18. X. He and L.-S. Luo, "Theory of the Lattice Bolztmann Equation: From Boltzmann Equation to Lattice Boltzmann Equation," *Physics Rev. E*, vol. 56, no. 6, Dec. 1997, pp. 6811–6817.
19. O. Filippova and D. Hänel, "Grid Refinement for Lattice-BGK Models," *J. Computational Physics*, vol. 147, no. 11, Nov. 1998, pp. 219–228.
20. F. Mazzocco et al., "Multiscale Lattice Boltzmann Schemes: A Preliminary Application to Axial Turbomachine Flow Simulations," *Int'l J. Modern Physics C*, vol. 11, no. 2, Mar. 2000, pp. 233–245.
21. O. Filippova et al., "Multiscale Lattice Boltzmann Schemes with Turbulence Modeling," *J. Computational Physics*, vol. 170, no. 2, July 2001, pp. 812–829.
22. F. Nannelli and S. Succi, "The Lattice Boltzmann Equation in Irregular Lattices," *J. Statistical Physics*, vol. 68, nos. 3–4, Aug. 1992, pp. 401–407.
23. X. He, L. Luo, and M. Dembo, "Some Progress in Lattice Boltzmann Method: Part I, Non-Uniform Grids," *J. Computational Physics*, vol. 129, no. 2, Dec. 1996, pp. 357–363.
24. H.D. Chen, "Volumetric Formulation of the Lattice Boltzmann Method for Fluid Dynamics: Basic Concept," *Physical Rev. E*, vol. 58, no. 3, Sept. 1998, pp. 3955–3963.
25. G.W. Peng et al., "Finite Volume Scheme for the Lattice Boltzmann Method on Unstructured Meshes," *Physical Rev. E*, vol. 59, no. 4, Apr. 1999, pp. 4675–4682.
26. O. Filippova and D. Hänel, "Acceleration of Lattice-BGK Schemes with Grid Refinement," *J. Computational Physics*, vol. 165, no. 2, Dec. 2000, pp. 407–427.
27. H. Chen, C. Teixeira, and K. Molvig, "Realization of Fluid Boundary Conditions via Discrete Boltzmann Dynamics," *Int'l J. Modern Physics C*, vol. 9, no. 8, Dec. 1998, pp. 1281–1292.
28. C.M. Rhie and W.L. Chow, "Numerical Study of the Turbulent Flow Past an Airfoil with Trailing Edge Separation," *AIAA J.*, vol. 21, no. 11, 1983, pp. 1525–1532.
29. D. Coles and A.J. Wadcock, "Flying Hot-Wire Study of Flow Past an NACA 4412 Airfoil at Maximum Lift," *AIAA J.*, vol. 17, no. 4, 1979, pp. 312–329.
30. S. Succi et al., "Chemical Efficiency of Reactive Microflows with Heterogeneous Catalysis: A Lattice Boltzmann Study," to be published in *European J. Applied Physics*.
31. S. Succi et al., "An Integer Realization of a Lax Scheme for Transport Processes in Multiple Component Flows," *J. Computational Physics*, vol. 152, no. 2, July 1999, pp. 493–516.
32. E. Oran and J. Boris, *Numerical Simulation of Reactive Flows*, Elsevier Science, New York, 1987.
33. M. Silverberg, A. Ben-Shaul, and F. Rebenstrost, "On the Effects of Adsorbate Aggregation on the Kinetics of Surface Reactions," *J. Chemical Physics*, vol. 83, no. 12, Dec. 1985, pp. 6501–6513.
34. M. Seel, "Modeling of Solid Rocket Fuel: From Quantum Chemistry to Fluid Dynamic Simulations," Computers in Physics, vol. 5, no. 5, Sept./Oct. 1991, p. 460.
35. A.F. Voter, "Hyperdynamics: Accelerated Molecular Dynamics of Infrequent Events," *Physical Rev. Letters*, vol. 78, no. 20, May 1997, pp. 3908–3911.

Sauro Succi is research director of the National Research Council's Institute of Applied Computing in Rome, Italy. His scientific interests cover a range of topics associated with the mathematical and computational modeling of complex system dynamics, including fluid turbulence, microhydrodynamics, quantum fluids, and discrete kinetic systems. He received a PhD in plasma physics from the Swiss Polytechnic Institute of Lausanne, Switzerland. Contact him at Istituto Applicazioni Calcolo, viale Policlinico 137, 00161, Roma, Italy; succi@iac.rm.cnr.it; www.iac.rm.cnr.it.

Olga Filippova is a researcher at the Institute of Combustion and Gas Dynamics at the University of Duisburg affiliated with the Aerodynamical Institute RWTH Aachen. Her scientific interests include the development and application of the Lattice Boltzmann method as a new efficient computational tool for studying low Mach number flows, in particular, turbulent and combustion flows in complex geometries. She received a PhD from Moscow State University, Russia. Contact her at the Institute of Combustion and Gasdynamics, Univ. Duisburg, 47048 Duisburg, Germany; olga@vug.uni-duisburg.de; www.vug.uni-duisburg.de/STAFF/worker-olga-main.html.

Greg Smith did his graduate work in the Physics Department of Harvard University, where he earned a PhD. He also worked as a postdoctoral fellow on multiscale modeling of materials. He is currently studying art at Hunter College, New York City. Contact him at gregory_sam_smith@yahoo.com.

Efthimios Kaxiras is a professor of physics and the Gordon McKay Professor of Applied Physics in the Physics Department and the Division of Engineering and Applied Sciences at Harvard University. His research interests include the physics of solids, surfaces, clusters, and macromolecules, studied by first-principles electronic structure methods. More recently, he has been involved in incorporating such methods in multiscale modeling of materials properties. He received a PhD in physics from MIT. Contact him at Lyman Laboratory, Physics Dept., Harvard Univ., Cambridge MA 02138; kaxiras@physics.harvard.edu; http://kriti.harvard.edu.